

# Artificial Intelligence Assists Discovery of Reaction Coordinates and Mechanisms from Molecular Dynamics Simulations

Hendrik Jung,<sup>1,\*</sup> Roberto Covino,<sup>1,\*</sup> and Gerhard Hummer<sup>1,2,†</sup>

<sup>1</sup>*Department of Theoretical Biophysics, Max Planck Institute of Biophysics, 60438 Frankfurt am Main, Germany.*

<sup>2</sup>*Institute of Biophysics, Goethe University, 60438 Frankfurt am Main, Germany.*

Exascale computing holds great opportunities for molecular dynamics (MD) simulations. However, to take full advantage of the new possibilities, we must learn how to focus computational power on the discovery of complex molecular mechanisms, and how to extract them from enormous amounts of data. Both aspects still rely heavily on human experts, which becomes a serious bottleneck when a large number of parallel simulations have to be orchestrated to take full advantage of the available computing power. Here, we use artificial intelligence (AI) both to guide the sampling and to extract the relevant mechanistic information. We combine advanced sampling schemes with statistical inference, artificial neural networks, and deep learning to discover molecular mechanisms from MD simulations. Our framework adaptively and autonomously initializes simulations and learns the sampled mechanism, and is thus suitable for massively parallel computing architectures. We propose practical solutions to make the neural networks interpretable, as illustrated in applications to molecular systems.

## I. INTRODUCTION

Computational molecular sciences face two outstanding challenges. On the one hand, ever growing computational power and sophisticated software enable us to simulate increasingly complex systems over ever longer times, resulting in massive trajectories that we are ill-equipped to process and interpret. Indeed, we still micromanage the data production process and rely on visual inspection by human experts to analyze long simulated trajectories. On the other hand, a small integration time step and upper bounds to the scalability of distributed calculations severely limit the sampling of interesting phenomena in extensive molecular dynamics (MD) simulations. Indeed, these phenomena are often rare events [1], stochastic transitions between metastable states that are separated by exponentially longer waiting times. Exascale supercomputers are going to further exacerbate the interpretation problem and, due to the slowing down of Moore’s law and the “Communication Wall”, fail to fully solve the sampling problem. Two strategies are available to speed up the sampling [2]: use of an unphysical bias in a single MD simulation to steer the dynamics of the system along a desired direction; or use of an ensemble of short judiciously initialized unbiased trajectories to enhance the sampling of transition paths (TPs) between metastable states. The TPs of rare events provide invaluable mechanistic insight into the investigated systems. Often these strategies either completely rely on, or can greatly profit from, the previous knowledge of a reaction coordinate (RC) [3, 4], which is a function of the configuration space that provides a condensed yet accurate description of the relevant dynamics of the system.

The interpretation and sampling problems are two faces of the same coin, since learning the salient features of a rare event, its RC, also enables us to effectively enhance its sampling. The two problems can therefore be tackled at the same time. However, finding a good RC is extremely challenging, even for relatively simple dynamical systems. Moreover, the search for RCs still almost entirely relies on direct human analysis, through visual inspection and tedious trial and error approaches, which are potentially biased and frequently fail to achieve satisfactory results. This dependence on human experts to initialize and interpret MD simulations threatens to become one of the main bottlenecks in the exascale computing era. We therefore need to develop tools able to perform the same tasks with minimal human intervention.

Trajectories produced by MD simulations are complex and high-dimensional data, containing subtle patterns that are scarcely identifiable by human operators, but can be efficiently identified by machine learning [5] and in particular deep learning [6, 7] approaches. In fact, specialized deep learning algorithms vastly out-compete humans in an increasing number of complex data intensive tasks. One of the challenges, however, is to translate the underlying patterns into a human understandable form [6].

Here, we show how combining advanced sampling schemes, maximum likelihood inference, and deep learning allows us to tackle the sampling and interpretation problems simultaneously, and to move towards the goal of autonomous production and interpretation of MD simulations of rare events. We take advantage of the power of Transition Path Sampling (TPS) introduced by Chandler, Dellago, Bolhuis, Geissler and collaborators [8, 9] to attempt simulations of transitions between metastable states. Unbiased simulations started at different initial configurations can, at the same time, be used to create a transition path ensemble [8, 9], and to estimate the committor [10], i.e., the probability that a simulation

\* These authors contributed equally to this work.

† Corresponding author: gerhard.hummer@biophysics.mpg.de

randomly initialized at a given configuration will evolve to one metastable state instead another [1, 4]. Inspired by the seminal work of Peters and Trout [11], we formulate the problem of learning the committor from the outcomes of the TPS simulation attempts as a statistical inference problem. Following the pioneering work by Ma and Dinner [12], we use the committor as a mapping between molecular configurations and the reaction mechanism, that we model by using artificial neural networks (ANN) [5]. By combining all these elements, we translate the problem of learning molecular mechanisms and RCs in a quantitative way to the problem of training an ANN on short simulations, which can be efficiently solved with the methods of deep learning.

We thus present a novel AI-assisted simulation algorithm that, in the spirit of reinforcement learning, iteratively and adaptively initializes and performs new MD simulations, and learns from the generated trajectories how to increase at every iteration the probability to observe rare transitions. With minimal human intervention, our algorithm finds the most efficient way to sample a rare molecular event by learning the underlying molecular mechanism and the corresponding RC, or, equivalently, learns the RC of a rare molecular event by sampling it numerous times. Therefore, we will ultimately obtain not only an unbiased ensemble of transition trajectories but also the underlying RC encoded in the trained ANN.

In the following, we will introduce the main elements of our method and illustrate its application on a model system. We will then study a conformational change in the standard molecular benchmark system alanine dipeptide, and investigate the dissociation of ion pairs in a concentrated solution of lithium chloride in water.

## II. ALGORITHM

The framework we introduce is valid for transitions among an arbitrary number of metastable states. However, for the sake of clarity, we will focus in the following on transitions between two states  $A$  and  $B$  (Figure (1)).

Taking advantage of TPS, we use short unbiased trajectories to generate an equilibrium ensemble of TPs between  $A$  and  $B$ . Given a path in configuration space connecting the two states, we initialize MD simulations from a configuration  $\mathbf{x}_{\text{sp}}$  lying on the path, and iteratively attempt to simulate TPs by using the so called ‘‘shooting move’’ [13]: we redraw velocities  $\mathbf{v}$  from the Maxwell-Boltzmann distribution and start independent simulations from the configuration  $\mathbf{x}_{\text{sp}}$ , forward with velocities  $\mathbf{v}$ , and backward with velocities  $-\mathbf{v}$ . Each simulation is stopped as soon as the trajectory enters one of the two states. There can be three possible outcomes: both forward and backward trajectories reach  $A$ , or they both reach  $B$ , or they reach different states,  $A$  and  $B$ , or  $B$  and  $A$ . In this last case, we can concatenate the forward

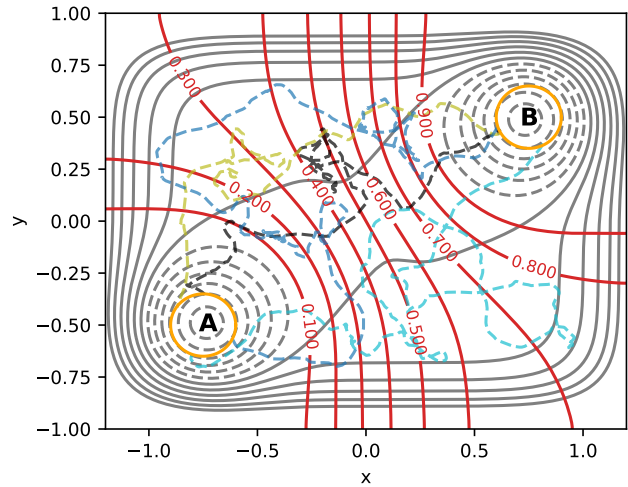


Figure 1. Model potential  $V(x, y)$  (Eq. 1 SI) with two metastable states  $A$  and  $B$ , defined as circles of radius  $r = 0.15$  centered on the minima (orange). The two states are separated by an approximately  $7 \text{ k}_B\text{T}$  high barrier and a broad barrier region. Isolines of the energy surface (grey) are separated by  $0.7 \text{ k}_B\text{T}$ . Isolines of the exact committor  $p_B(x, y)$  in steps of  $0.1$  are shown as solid red curves. The dashed colored lines connecting  $A$  and  $B$  represent TPs of varying length simulated by Langevin dynamics.

and reversed backward trajectories and form a TP  $\chi$ . We iterate this sampling scheme by varying the starting configuration. Each shooting move  $i$  is summarized by its starting configuration, and the number of trajectories  $n_X^{(i)}$  ending in states  $X = A$  and  $B$ , i.e., by the set of parameters  $\theta^{(i)} = \{\mathbf{x}_{\text{sp}}^{(i)}, n_A^{(i)}, n_B^{(i)}\}$ , with  $n_A^{(i)} + n_B^{(i)} = n^{(i)}$ . In the following, without loss of generality we will consider  $n^{(i)} = 2$ . We then build the TP ensemble by accepting simulated TPs based on a Metropolis-Hastings criterion [13] (Eq. 2 SI).

The outcome of statistically independent shooting moves follows a binomial distribution. Therefore, each shooting move is described by the likelihood function  $L[p_B(\mathbf{x}_{\text{sp}}) | n_A, n_B] \propto [p_B(\mathbf{x}_{\text{sp}})]^{n_B} [1 - p_B(\mathbf{x}_{\text{sp}})]^{n_A}$ , where  $p_B(\mathbf{x}_{\text{sp}})$  and  $p_A(\mathbf{x}_{\text{sp}}) = 1 - p_B(\mathbf{x}_{\text{sp}})$  are the probabilities that a trajectory initialized at  $\mathbf{x}_{\text{sp}}$  with random velocities will first enter state  $A$  and  $B$ , respectively. For statistically independent trajectories, the quantity  $p_B(\mathbf{x}_{\text{sp}})$  is known as the splitting probability or committor of state  $B$  [4]. In our likelihood formulation, we tacitly assume that the outcome, in terms of the state first reached, for two trajectories initiated from a common shooting configuration is independent of the respective initial velocities.

The committor ranges from  $p_B(\mathbf{x} \in A) = 0$  to  $p_B(\mathbf{x} \in B) = 1$ , and maps all configurations in the transition region to an intermediate value (Figure 1). The foliation of level sets of the committor monitors the progress along the transition  $A \rightarrow B$ , and therefore provides a general and rigorous way to quantify the mechanism de-

scribed by such a transition [1, 4, 12, 14–16]. Consequently, the direction orthogonal to the foliation along the most probable configurations defines the optimal RC of the transition  $A \rightarrow B$  (Figure 1). Without loss of generality we model the RC  $q(\mathbf{x})$  by parametrizing the committor as

$$p_B(\mathbf{x}) \equiv p_B[q(\mathbf{x})] = \left[1 + e^{-q(\mathbf{x})}\right]^{-1}. \quad (1)$$

The RC is at this point an unknown scalar dimensionless function  $q(\mathbf{x})$ , which will be in general a complex nonlinear function of the coordinates of the system. Eq. (1) ensures that the committor ranges between 0 and 1 for any value of the RC. Also,  $p_B[q(\mathbf{x}) = 0] = 1/2$  defines the transition state ensemble (TSE) for transitions between two states.

We model the unknown RC  $q(\mathbf{x})$  with an ANN [5]. ANNs are flexible and powerful tools to model highly nonlinear functions and reproduce complex patterns in high-dimensional data, and, after the first pioneering approaches [12, 17], were recently at the center of several important advancements in the field of biomolecular simulations [18–28]. We thus write the unknown RC as  $q(\mathbf{x}) = q_{\text{ANN}}(\mathbf{x}|\mathbf{w})$ , where the weight matrix  $\mathbf{w}$ , i.e., the fitting parameters of the ANN, defines the connections between nodes (see Figure 1 and Eq. 3 in the SI for the explicit definition).

After  $N$  statistically independent shooting moves, the total likelihood as a function of the proposed RC will be

$$L_{\text{tot}}[q_{\text{ANN}}(\mathbf{x}_{\text{sp}}|\mathbf{w})|n_A, n_B] \propto \prod_{i=1}^N \left[ p_B \left[ q_{\text{ANN}}(\mathbf{x}_{\text{sp}}^{(i)}|\mathbf{w}) \right] \right]^{n_B^{(i)}} \times \left[ 1 - p_B \left[ q_{\text{ANN}}(\mathbf{x}_{\text{sp}}^{(i)}|\mathbf{w}) \right] \right]^{n_A^{(i)}} \quad (2)$$

Combining equations (1) and (2) we obtain the loss function

$$l(\mathbf{w}|\boldsymbol{\theta}) \equiv -\log L_{\text{tot}}[q_{\text{ANN}}(\mathbf{x}_{\text{sp}}|\mathbf{w})|n_A, n_B] = \sum_{i=1}^N \left[ n_B^{(i)} \log \left( 1 + e^{-q_{\text{ANN}}(\mathbf{x}_{\text{sp}}^{(i)}|\mathbf{w})} \right) + n_A^{(i)} \log \left( 1 + e^{q_{\text{ANN}}(\mathbf{x}_{\text{sp}}^{(i)}|\mathbf{w})} \right) \right], \quad (3)$$

where  $\boldsymbol{\theta} = \left\{ \mathbf{x}_{\text{sp}}^{(i)}, n_A^{(i)}, n_B^{(i)} \right\}_{i=1, \dots, N}$  is the training set acquired over  $N$  shooting moves. We therefore train the ANN, i.e., we fit the weight matrix  $\mathbf{w}$ , by minimizing the loss function Eq. (3) on the training set  $\boldsymbol{\theta}$ , and obtain  $\hat{q}_{\text{ANN}}(\mathbf{x}|\mathbf{w})$ , a maximum likelihood estimator of the RC and consequently of the committor.

Recapitulating, the algorithm proceeds in the following way (Figure 2). (0) The only required input is the definition of the metastable states  $A$  and  $B$  as a function of some order parameters. We then initialize  $q_{\text{ANN}}(\mathbf{x}|\mathbf{w})$  by randomly assigning values to the weight matrix  $\mathbf{w}$ .

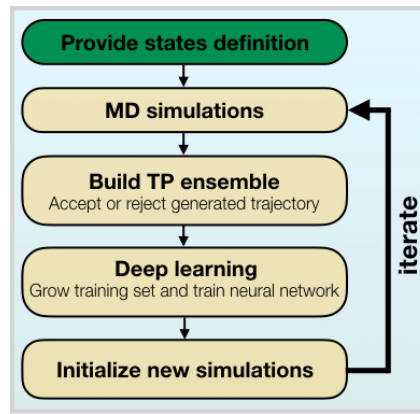


Figure 2. Schematic flow chart of the AI-assisted MD simulations algorithm.

Given an initial path  $\chi^{(0)}$  connecting states  $A$  and  $B$ , we randomly select the first shooting configuration  $\mathbf{x}_{\text{sp}}^{(1)}$ . (1) For every step with  $i > 0$ , we perform a shooting move from  $\mathbf{x}_{\text{sp}}^{(i)}$ , generating velocities from a Maxwell-Boltzmann distribution and propagating the dynamics forward and backward, and append the outcome  $\boldsymbol{\theta}^{(i)}$  to  $\boldsymbol{\theta}$ . (2) If we sample a new TP,  $\chi^{(i)}$ , we accept or reject it following a Metropolis-Hastings criterion [13] (Eq. 2 SI). (3) We minimize the loss function Eq. (3) on the training set  $\boldsymbol{\theta}$ , which contains all  $\boldsymbol{\theta}^{(i)}$  stored so far, and obtain  $\hat{q}_{\text{ANN}}^{(i)}(\mathbf{x}|\mathbf{w})$ . (4) We select a new shooting configuration  $\mathbf{x}_{\text{sp}}^{(i+1)}$  from  $\chi^{(i)}$ , the last TP added to the ensemble, by using the (Cauchy-Lorentz) selection probability

$$p_{\text{sel}}(\mathbf{x}|\chi^{(i)}, \mathbf{w}, \gamma) \propto \frac{\gamma^2}{\hat{q}_{\text{ANN}}^{(i)}(\mathbf{x}|\mathbf{w})^2 + \gamma^2}, \quad (4)$$

which describes a fat-tailed distribution centered around  $\hat{q}_{\text{ANN}}^{(i)}(\mathbf{x}|\mathbf{w}) = 0$ , where  $\gamma > 0$  is the scale parameter. We iterate steps (1) to (4) until we obtain convergence of the TP ensemble.

The algorithm adaptively creates its own training set, which will grow at every iteration, and the ANN will be trained both on successes and failures. The acquired information is then used in Eq. (4), which ensures that  $\mathbf{x}_{\text{sp}}^{(i+1)}$  is distributed around  $\mathbf{x}^{\text{TSE}(i)}$ , i.e., the best estimate of the TSE given the available training data. Hence, crucially, at every step the algorithm makes full use of all available information to autonomously and adaptively initialize new MD simulations and to optimize the probability to sample new TPs.

Learning the RC and generating the equilibrium TP ensemble converge in an orchestrated fashion. During training, the loss function Eq. (3) initially oscillates and then converges, i.e., the ANN converges to an optimal weight matrix  $\mathbf{w}^{\text{opt}}$  that can reproduce all future observations  $\boldsymbol{\theta}^{(i)}$ . Consequently, at this point we have learned the optimal RC describing the dynamics of the rare event, encoded in the ANN and defined by

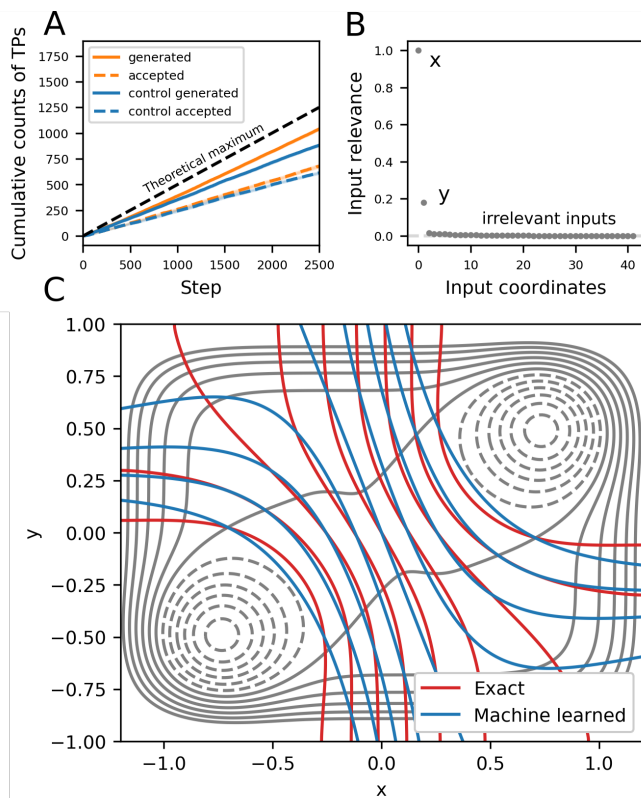


Figure 3. Results for 42-dimensional model system of Figure 1. (A) Cumulative count of generated (continuous line) and accepted (dashed line) TPs in AI-assisted MD simulations (orange) and standard control TPS (blue) performed on the model energy surface shown in Figure 1. Each line shows the average over 10 independent runs. The standard error of the mean is smaller than the thickness of the lines. The black dashed line represent the theoretical maximum for generation of TPs. (B) Input relevance analysis. All 42 input coordinates are ranked according to their normalized relevance. (C) Comparison between the level sets of the exact (red) and machine learned (blue) committor  $p_B(x, y)$ . Isolines are shown in intervals of 0.1 between 0.1 and 0.9.

$\hat{q}_{\text{ANN}}^{\text{opt}}(\mathbf{x}|\mathbf{w}) \equiv \hat{q}_{\text{ANN}}(\mathbf{x}|\mathbf{w}^{\text{opt}})$ , which enables the generation of new TPs with high efficiency. Convergence of the TP ensemble can be slower and must be monitored separately, e.g., by tracking the convergence of some physical parameters such as the TP time. As in similar schemes, if the initial path is very far from the equilibrium TP ensemble, it might be necessary to discard the TPs sampled during an initial equilibration phase.

We illustrate each step of our algorithm by studying a 42-dimensional model system described by the instantaneous configuration  $\mathbf{x}(t) \in \mathbb{R}^{42}$ . Here,  $x_1 = x$  and  $x_2 = y$  evolve by Langevin dynamics on the energy potential  $V(x, y)$  shown in Figure 1, which combines the challenges of having two metastable states separated by a 7 k<sub>B</sub>T high barrier and a broad barrier region. For each  $j > 2$ , instead, the nuisance coordinate  $x_j$  evolves by Langevin dynamics on the harmonic potential  $V_j(x_j) = \omega_j^2 x_j^2 / 2$ ,

with random angular frequencies  $\omega_j$ . Even though only  $x$  and  $y$  contribute to the RC, we challenge our deep learning approach by training the ANN on the full 42-dimensional input space.

Our algorithm samples TPs with probability close to 50%, which is the theoretical upper limit [10] assuming statistically independent shooting moves (Figure 3). Also, it tends to perform better than the already efficient standard TPS approach, in which initial configurations  $\mathbf{x}_{\text{sp}}^{(i+1)}$  are selected with uniform probability from the last accepted TP.

At convergence, our algorithm does not only return the correct equilibrium TP ensemble but also the RC describing the transition, which is encoded in  $\hat{q}_{\text{ANN}}^{\text{opt}}(\mathbf{x}|\mathbf{w})$ . This is a complex function that cannot be immediately interpreted in a simple way. We can of course always visually inspect the TSE defined by  $\hat{q}_{\text{ANN}}^{\text{opt}}(\mathbf{x}^{\text{TSE}}|\mathbf{w}) = 0$ , which can be trivially extracted from the sampled TPs. Importantly, the quantitative information contained in the trained ANN can be mapped on the Cartesian coordinates of molecular structures to provide direct visual insight in the reaction mechanism. Indeed, we can highlight each atom  $n$  according to its contribution to the RC by evaluating the (normalized) magnitude of the gradient of the ANN in the TSE, i.e.,

$$c_n = \frac{\left| \nabla_{\mathbf{x}_n^{(\text{cart})}} \hat{q}_{\text{ANN}}^{\text{opt}}(\mathbf{x}^{\text{TSE}}|\mathbf{w}) \right|}{\left| \sum_m \nabla_{\mathbf{x}_m^{(\text{cart})}} \hat{q}_{\text{ANN}}^{\text{opt}}(\mathbf{x}^{\text{TSE}}|\mathbf{w}) \right|}, \quad (5)$$

which can be calculated by a straightforward application of the chain rule (backpropagation).

Additionally, we propose a solution to approximately extract the information encoded in the ANN and translate it to a human friendly explicit formula. Not all input coordinates  $\mathbf{x}$  contribute equally to the RC. In order to identify the most relevant ones, we build on the procedure reported in [29]. We quantify the information carried by the  $j$ -th input coordinate by resampling the loss function (Eq. (3)) replacing one by one each input coordinate  $x_j$  with random uninformative values. Finally, we rank each input coordinate  $x_j$  by the normalized increase in loss caused by their replacement with noise (Figure 3). This analysis correctly reveals that only two input coordinates actually determine the output of the ANN, corresponding to  $x$  and  $y$ .

We can now use symbolic regression [30, 31] to automatically build a mathematical expression  $q_{\text{sr}}(x, y)$  that approximately reproduces the machine learned optimal RC  $\hat{q}_{\text{ANN}}^{\text{opt}}(\mathbf{x}|\mathbf{w})$ . Symbolic regression finds the best fit to a given data set searching both model and parameter space by genetic programming, evolving combinations of elementary functions and input variables through random mutations and survival of the fittest [31]. Applied to our model system with input variables  $(x, y)$ , symbolic regression produces a simplified RC,  $q_{\text{sr}}(x, y) = (3.32x + 1.24y) \exp(2.92xy)$ , which corresponds to a committor in excellent agreement with the



exact one (Figure 3). Indeed, the simplified RC not only captures the linearity of the committor close to the TSE but also the curvature close to the metastable states. Clearly, high energy regions of the surface are not sampled by the MD engine and display a less significant agreement.

### III. APPLICATION TO MOLECULAR SYSTEMS

In order to use deep learning to study molecular rare events we must first decide how to represent molecular systems. Here we face the trade off between the generality of the representation and finite sampling. Indeed, it would be possible to use cartesian coordinates as input for the ANN, but we assume that the systems to simulate will be challenging, and hence the amount of training data scarce. Therefore, we will choose general molecular representations that make use of all previous knowledge already available, e.g., by satisfying the physical symmetries of the system. For instance, molecular configurations can be described by using internal coordinates [32], i.e., all bonds, angles, and dihedrals that can be built with a set of atomic positions. Internal coordinates are in a one-to-one mapping with cartesian ones, but are manifestly invariant w.r.t. global rotations and translations.

A molecular rare event is often modulated by its environment, water in the simplest case, which should be included in the molecular representation as well. In the following we will label a “solute” the part of the system undergoing the rare transition, and a “solvent” its environment. The solvent is invariant under the permutation of identical particles. We will describe the solvent by using a modification of symmetry functions introduced by Behler, Parrinello [17, 19, 33], Geiger and Dellago [18], which are a general way to describe the spatial organization of molecules around a specific atom. In particular, we will use two kind of symmetry functions,  $G_i^2$  and  $G_i^5$  (Eq. (6) and (8)). The first quantifies the density of solvent molecules at a given radial distance from a specific solute atom; the second quantifies the isotropy of the angular distribution of solvent molecules at a given radial distance around a solute atom. These representations are not only invariant w.r.t. global translations and rotations but also w.r.t. exchange of solvent molecules.

#### A. Conformational change in benchmark peptide

We applied our computational framework to the prototypical benchmark peptide alanine dipeptide (*N*-acetyl alanine *N'*-methylamide) [34]. We investigated the thermally activated conformational change of the dihedral angle  $\psi$ , corresponding to trajectories crossing a large free energy barrier as shown in Figure 2 of the SI. The only required initial input are the metastable states, defined

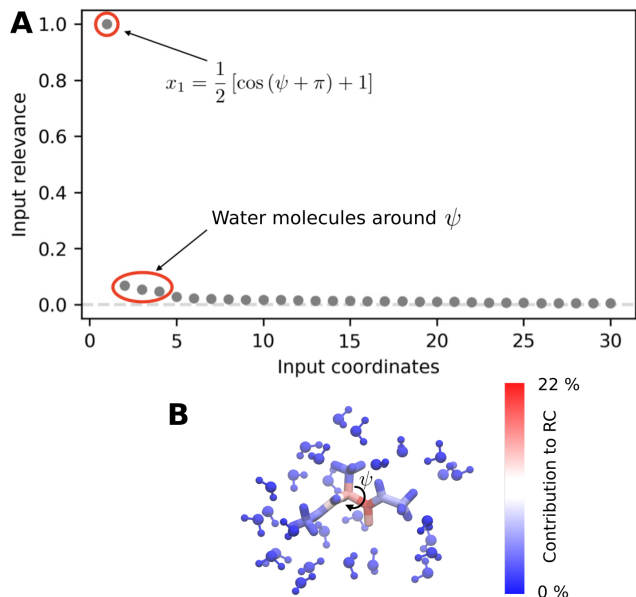


Figure 4. Input relevance analysis and visual representation of the machine learned RC for alanine dipeptide. (A) We show the normalized input relevance of the 30 most important input coordinates. The first point corresponds to the input coordinate  $x_1 = \psi \equiv \frac{1}{2} [\cos(\psi + \pi) + 1]$ . The following 3 points correspond to coordinates describing the organization of water molecules around the peptide. (B) Structure of alanine dipeptide extracted from a simulated TP that is predicted to be part of the TSE. Atomic coordinates are colored according to their contribution to the RC (Eq. (5); red most important, blue least important).

in this case as a function of the dihedral angles  $\phi$  and  $\psi$ . We simulated the system in explicit solvent, and used internal coordinates to describe the peptide configurations and symmetry functions to represent the solvent, using both as inputs for deep learning. Our framework enabled us to simulate TPs with high efficiency, and rapidly obtain an equilibrated TP ensemble (Figure 3 SI).

The input relevance analysis reported in Figure 4 correctly identifies the coordinate  $x_1 = \psi \equiv \frac{1}{2} [\cos(\psi + \pi) + 1]$  as the major descriptor of the conformational change. The analysis also highlights a marginal role for three further input coordinates describing the organization of water molecules around the peptide. In particular, these three coordinates describe the angular distribution of water oxygens at a distance of 0.175 nm from the oxygen of the acetyl involved in the peptide bond ( $x_2$ ), a hydrogen atom in the methyl-group ( $x_3$ ), and the nitrogen of the methylamide ( $x_4$ ) (Table I SI). Figure 4 shows a representative structure of the TSE, for which the ANN predicts a value of  $p_B = 0.5$  in excellent agreement with the  $p_B = 0.46$  value returned by a direct sampling of the committor using 10,000 trajectories. Each atom in the structure is colored according to its contribution to the RC, and a simple visual inspection immediately reveals the dominant aspect of the molecular mechanism.

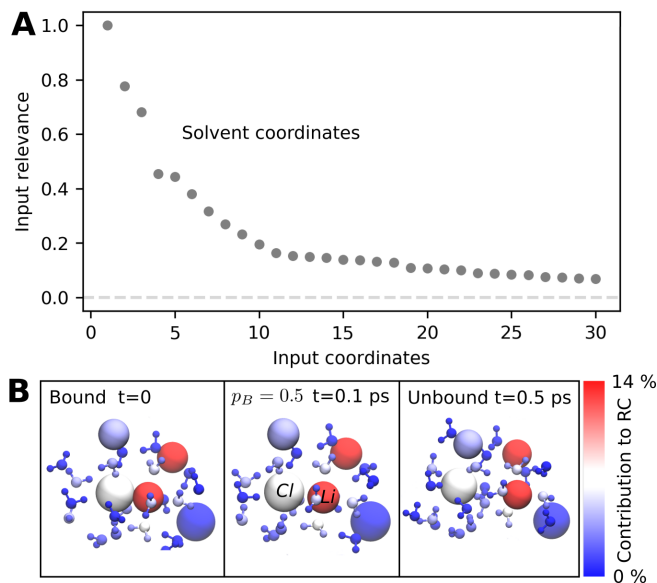


Figure 5. Input relevance analysis and visual representation of the machine learned RC for LiCl dissociation. (A) We report the normalized input relevance of the 30 most important input coordinates, which all describe the collective distribution of the solvent around the dissociating ion pair. (B) Configurations extracted from a simulated TP, in the bound state, from the TSE, and in the unbound state. The dissociating ion pair is shown at the center and labeled (small spheres:  $\text{Li}^+$ ; large spheres:  $\text{Cl}^-$ ). Atomic coordinates are colored according to their contribution to the RC (Eq. (5); red most important, blue least important).

We then used the four most relevant input coordinates to approximate the trained ANN by a simple function. Depending on the desired level of regularization we obtained slightly different expressions (Table II SI). The optimal is  $q_{\text{sr}}(\tilde{\psi}, x_3) = -8.38\tilde{\psi} + 5.62 \exp(-0.285x_3)$ , which evaluated on the training data returns a loss of 1.051 compared to 1.031 for the full ANN.

## B. Ion dissociation in water

We then investigated the dissociation of lithium and chloride ions in a 1 M solution. Despite its apparent simplicity, understanding this reaction in quantitative terms poses a challenge [35], because it is governed by many-body long range interactions and by instantaneous collective motions of all surrounding water molecules and ions. We focused on a specific pair of ions, and used their distance  $r$  as a parameter to define bound and unbound states. We then described the remaining part of the solution with symmetry functions of the positions of all other lithium and chloride ions, and the oxygen of water molecules. Our AI-assisted simulation framework produces TPs significantly more efficiently than a standard TPS implementation (Figure 4 SI).

The input importance analysis reveals that indeed the environment controls the dissociation reaction (Figure 5 and Table III SI). Contrary to the previous application, there is no single dominant descriptor of the reaction. The trained ANN employs a large number of input coordinates, and their importance decays in a power-law fashion. Of the 10 most relevant coordinates, most probe the density and angular distribution of lithium and chloride counter-ions around the dissociating ion pair, while only one probes the distribution of water molecules (Table III SI). Notably, in independent runs we obtain alternative “mirror” symmetry functions, where lithium and chloride exchange, which means that the ANN can use alternative descriptions of analogous configurations. Also, the interatomic distance of the dissociating pair never appears among the most important input coordinates. Figure 5 shows representative configurations along a TP, including a configuration of the TSE identified by the trained network, for which a direct sampling of the committor with 1,000 simulations returns  $p_B = 0.53$ . The structures are colored according to the contribution of each atom to the RC, and immediately reveal the many-body character of the mechanism and its main features. Indeed, we can clearly see 4 water molecules coordinating the central lithium ion and 2 distant competing lithium counter-ions.

Distilling a simple equation from the full network is in this case more challenging. By using the 10 most relevant input coordinates identified in Figure 5, we obtained expressions that do not correctly reproduce the committor of the reaction. This is possibly due to an insufficient number of input coordinates. We obtained accurate expressions by using the first 10 coordinates and the interatomic distance  $r$  of the dissociating ion pair. Depending on the regularization, we obtained a number of different expressions that all offer an insightful physical interpretation (Table IV SI). As an example, we report  $q_{\text{sr}}(r, x_1, x_9) = 29.5r - 8.19 \exp(-0.87x_1) - 0.29x_9$ , where  $x_1$  describes the angular distribution of distant ( $\sim 0.7$  nm) chloride counter-ions and  $x_9$  describes the angular distribution of close ( $\sim 0.175$  nm) water molecules around the dissociating lithium ion.

## IV. DISCUSSION

The computational framework we introduced enhances the simulation of rare events with little previous knowledge and minimal human intervention. Given two metastable states defined with some arbitrary order parameters, the algorithm efficiently simulates rare events by learning the underlying reaction mechanism, using only adaptively initialized short and unbiased simulations. In the spirit of reinforcement learning [5], our framework autonomously builds its own training set, training both on successes and failures. We combine a number of established techniques in a very general way, such that each building block might be exchanged with a

potentially more suitable alternative. This could involve the sampling strategy [36–38]; performing MD simulations at atomistic or coarse-grained resolution; considering more sophisticated inference models and integrating experimental information in a systematic way; exploiting alternative network architectures and different regression schemes for the learning phase [39].

At convergence, the algorithm returns an equilibrium ensemble of simulated TPs and a functional form of the committor encoded in an ANN, which is both differentiable and inexpensive to evaluate. We therefore obtain a very efficient way to calculate the committor of molecular configurations, which can be used to identify level sets of the committor from the sampled TPs by straightforward evaluation and bookkeeping. Given that these structures belong to unbiased trajectories guarantees that the committor is evaluated only in the relevant regions of the configuration space. Molecular configurations belonging to the level sets can then immediately be used to further characterize the transition with methods like milestoneing [40], forward-flux-sampling [41], and s-shooting [38].

Despite its crucial role in controlling molecular mechanisms, we often neglect the environment in which a rare event takes place, mostly because we struggle to capture many-body interactions. By processing large amounts of input coordinates, machine learning offers the potential to systematically describe even complex biomolecular environments, like dense solutions or complex lipid bilayers.

We proposed a solution to make the trained network interpretable, by approximating the ANN with a simple function of the few input coordinates that actually control the transition. The resulting equation is an accurate approximation of the RC that can be used to calculate the free energy surface governing the transition and its kinetics by using techniques like umbrella sampling [42, 43], metadynamics [44], and within the framework of TPS itself [16]. The analytic form of the RC also provides a starting point to inspire and build physical analytic theories. Any previous knowledge can be easily integrated with the generated equation, simply by imposing any relevant coordinate or functional form that one wants to appear in the reduced RC representation. Additionally, visualizing the contribution to the RC with automatically generated annotated structures is a powerful tool to gain insight in the reaction mechanism (Figure 4 and 5). The AI autonomously generates images guiding human operators in understanding the discovered mechanism, making the ANN interpretable in a very immediate way.

The resampling procedure to identify the important input coordinates is particularly effective when those have a physical meaning. However, for challenging problems we will usually use coordinates that are agnostic and redundant. We expect that in these cases the resampling procedure will return a power-law spectrum, similar to what we observe in Figure 5, and extracting few essential input coordinates will be challenging. This highlights the importance of developing representations of given classes of systems general enough to be transferable within the

same class [45, 46]. Similarly to other recent strategies, we can easily feed a large list of features (“collective variables”) to our algorithm [47]. Another route to follow is to combine deep learning and similar methods with manifold learning techniques [23].

Future versions of the algorithm will benefit from the ongoing research in the field of interpretable ANN. In particular, we will explore the possibility that networks trained on molecular events learn a hierarchy of features of the systems, similarly to what happens with hierarchical networks used in the field of image processing. One strategy is to map back the contribution of each layer of a deep network to molecular structures. These hierarchical features could be used to engineer transferable representations used as inputs for other problems, as discussed above.

An optimal definition of the metastable states is an important aspect to avoid wasting computational resources, and can be improved within the present framework in an iterative way. One can start with a very conservative definition, and then merge regions of the configuration space that the network, trained on quick exploratory runs, estimates being strongly committed to either one of the states.

The algorithm can be easily generalized to study rare transitions between multiple states. This is straightforward if the states are known in advance, since it suffices to consider a multi-state TPS [48] and definition of the committor [49] and to use a multinomial equivalent of Eq. (1), i.e., a softmax function. With the same approach we can treat trajectories that will not commit during the available simulation time because of unknown states or long-lived intermediates, which can be identified and characterized in post-processing. Simulations that do not commit because of extremely long TP times, instead, will require a staged approach and an opportune modification of the inference model.

Controlling the balance between exploitation and exploration is straightforward in our framework. Maximum efficiency of generating TPs (exploitation) is obtained when the network initializes new trajectories close to the TSE, which occurs when the selection probability in Eq. (4) is sharply peaked about the TSE. An ideal RC, however, should explain the transition not only close to the TSE but also in all other regions of the reaction, and in particular close to the boundaries of the metastable states. Exploration can thus be prioritized by a flatter selection probability that increases the probability to initialize trajectories far from the TSE.

Tuning the selection probability to initialize trajectories away from the TS, and also within the metastable states, facilitates the discovery of additional reaction channels and therefore alternative mechanisms within the same exploratory run. Alternatively, one could train two or more independent networks in parallel. Comparing the losses evaluated by the first network on configurations sampled by the second one – and vice versa – will reveal whether the two networks have indeed sampled

the same mechanism. Furthermore, we will explore more systematic ways of discovering multiple mechanisms by using multi-domains networks and inference schemes [50].

Our algorithm shares with other data-driven learning approaches the challenges of avoiding overfitting and of validating the learned results. The committor, which is ultimately what the ANN will learn, can always be validated in an expensive yet straightforward direct sampling. This will not be an option, however, for systems that are extremely expensive to simulate, for which more advanced strategies are required, like designing novel training schemes that intervene only when new "unusual" configurations are sampled, and using ANN with built-in regularizations. However, overfitting is not a serious issue for the production of data, and could be avoided in a thorough post-processing to learn the RC.

Regarding scalability the algorithm is already almost trivially parallelizable. Indeed, all the deep learning machinery can be concentrated on a single master node, which at every iteration communicates initial configurations to other nodes in the network, harvests the outcome of the performed simulations, and trains the artificial neural network on the resulting new data. Since every step of this distributed calculation satisfies detailed balance, the resulting sets of simulated TPs can simply be combined to obtain an equilibrium ensemble. This feature potentially solves the challenge of efficiently scaling simulations of rare events on large supercomputers.

In conclusion, we introduced a novel AI-assisted computational framework that represents a step forward towards the goal of automatic design, execution, and interpretation of MD simulations of rare events. This framework simultaneously enables the enhancement of sampling, the discovery of reaction mechanism, and the learning of the corresponding reaction coordinate, thereby opening the door to simulations of complex molecular events that are currently unfeasible. Our algorithm has the potential to transform MD simulations of rare and interesting molecular events into a semi-autonomous high-throughput technique, capable of scaling efficiently on exascale supercomputers. Using reinforcement learning to learn the committor is a very general idea, which can be potentially used to study any time-series of complex data that admits a forward commitment probability. The main challenge for the future will be to make the ANN systematically interpretable and distilling analytic representations – or even physical laws [30] – that describe the discovered molecular mechanism in a more human-accessible form.

## V. MATERIALS AND METHODS

### A. Model system

We simulated Langevin dynamics on the model energy landscape shown in Figure 1 described by Eq. 1 SI using the openpathsampling engine [51] and an integrator with

BAOAB splitting [52], with a timestep  $\Delta t = 0.02$  ns and friction  $\gamma = 2.5$  ns<sup>-1</sup>. We defined the states *A* and *B* as circles with a radius of  $r = 0.15$  centered on the two minima. Each additional independent nuisance coordinate  $x_i$  follows a harmonic potential with frequency  $\omega_i$ . The first two frequencies were chosen such that their periods are respectively larger and comparable to the average transition path time of  $\langle t_{TP} \rangle \approx 11$  ns. The remaining frequencies were chosen randomly from a uniform distribution in the interval  $[0 \text{ ns}^{-1}, 10 \text{ ns}^{-1})$ . All oscillator masses were set to  $m = 1$ . The initial TP is a straight line connecting the two stable states in the plane of the coordinates  $x$  and  $y$ . The exact committor reported in Figures 1 and 3 was obtained by solving the adjoint Fokker-Planck equation with a standard relaxation technique.

### B. Deep learning

We performed deep learning by training a self-normalizing ANN [53] with four hidden layers and a final layer with one node and a linear activation function. We used the "Lecun normal" initialization and applied a dropout of 10% after the last hidden layer [53]. We trained the ANN with the Adam gradient descent algorithm [54], training only after every second TPS step and using a learning rate of  $\text{lr} = 5 \cdot 10^{-4}$ . We interrupted the training process if the loss stayed almost constant and resumed it only upon a loss decrease. For the model system the number of nodes per layers equals the number of inputs, 42. For simulations of alanine dipeptide and LiCl dissociation it equals half the number of inputs, hence 750 and 264 nodes per layer, respectively. We performed all deep learning with custom written code based on keras [55].

### C. Input coordinate relevance analysis

For every  $j$ -th input coordinate we built the set  $\tilde{\theta}(j) = \left\{ \tilde{\mathbf{x}}_{\text{sp}}^{(i)}(j), n_A^{(i)}, n_B^{(i)} \right\}_{i=1, \dots, N}$ , where  $\tilde{\mathbf{x}}_{\text{sp}}^{(i)}(j)$  was obtained by replacing the  $j$ -th component of  $\mathbf{x}_{\text{sp}}^{(i)}$  with  $\tilde{x}_j^{(i)} \sim \mathcal{U}(\min(x_{j,\text{sp}}), \max(x_{j,\text{sp}}))$ , i.e., a random number uniformly distributed between the extreme values of  $x_{j,\text{sp}}$  over the whole training set  $\theta$ . We then defined the input relevance  $r(x_j) = \left[ l(\mathbf{w}^{\text{opt}} | \tilde{\theta}(j)) - l(\mathbf{w}^{\text{opt}} | \theta) \right]$ , which quantifies the impact of the lost information carried by the  $j$ -th input coordinate by resampling the loss function (3). This quantity is larger the more informative  $x_j$  is as an input coordinate. We normalized the input relevance by subtracting the converged loss of the unperturbed ANN and dividing all entries by the largest relevance. We then ranked each input coordinate  $x_j$  by the normalized  $r(x_j)$  and identified the most relevant ones.



## D. Symbolic regression

The implementation of the symbolic regression is based on the python package `dcgpy` [31], and alternates between genetic programming optimization and gradient based optimization of the constants. The fitness of each trial expression  $q_{\text{sr}}(\mathbf{z})$  is measured by  $l_{\text{sr}}(q_{\text{sr}}|\boldsymbol{\theta}) \equiv -\log L_{\text{tot}}[q_{\text{sr}}(\mathbf{z}_{\text{sp}})] + \lambda n_c$ , where  $\mathbf{z}$  is a subset of all input coordinates  $\mathbf{x}$ . We added the regularization term  $\lambda n_c$  in order to keep expressions simple and avoid overfitting, with  $\lambda > 0$  and  $n_c$  being a measure of the complexity of the trial expression.

## E. Molecular representation

In molecular systems one often distinguishes a solute and a solvent. We described configurations of the first by using internal coordinate [32], and the second by using a modification of previously introduced symmetry functions [17–19, 33]. The first one quantifies the density of solvent molecules around a solute atom  $i$  and is defined as:

$$G_i^2 = \sum_j e^{-\eta(r_{ij}-r_s)^2} f_c(r_{ij}), \quad (6)$$

where the sum runs over all solvent atoms  $j$  of a specific atom type,  $r_{ij}$  is the distance between the central atom  $i$  and atom  $j$ ,  $r_s$  is the distance from the central atom at which the shell is centered and  $\eta$  controls the width of the shell. The function  $f_c(r)$  is a Fermi cutoff defined as:

$$f_c(r) = \begin{cases} [1 + \exp(\alpha_c(r - r_c - 1/\sqrt{\alpha_c}))]^{-1} & r \leq r_c \\ 0 & r > r_c \end{cases}, \quad (7)$$

which ensures that the contribution of distant solvent atoms vanishes. The second type of symmetry function probes the angular distribution of the solvent in a shell around the central atom  $i$ :

$$G_i^5 = \sum_{j,k>j} [\lambda + \cos \vartheta_{ijk}]^\zeta e^{-\eta[(r_{ij}-r_s)^2 + (r_{ik}-r_s)^2]} \times \quad (8) \\ \times f_c(r_{ik}) f_c(r_{ij}),$$

where the sum runs over all solvent atom pairs,  $\vartheta_{ijk}$  is the angle spanned between the two solvent atoms and the central solute atom, the parameter  $\zeta$  must be an even number and controls the sharpness of the angular distribution, while the parameter  $\lambda$  is either  $+1$  or  $-1$  and controls whether the location of the minimum of the cosine bracket is at  $\vartheta_{ijk} = 0$  or at  $\vartheta_{ijk} = \pi$ . Training the ANN is facilitated if all inputs lie in a range between 0 and 1. We therefore used  $0.5(\cos(\phi)+1)$  for every angle  $\phi$ , and  $(0.5(\sin(\vartheta)+1), 0.5(\cos(\vartheta)+1))$  for every dihedral

angle  $\vartheta$ . We normalized the symmetry functions, dividing by the expected average number of atoms or pairs for an isotropic distribution in the probing volume.

## F. MD simulations

We simulated alanine dipeptide in the amber ff99SB-ILDN forcefield [56], with the termini capped by *N*-acetyl and *N*-methylamide groups, and solvated by 543 TIP3P water molecules [57].

We simulated a solution of lithium chloride in the Joung and Cheatham forcefield [58], using a cubic simulation box containing 37 lithium and 37 chloride ions, solvated with 2104 TIP3P water molecules, corresponding to a concentration of 1 M LiCl.

We performed all MD simulations using the openMM MD engine [59], with a velocity Verlet integrator with velocity randomization [60] from the python package `openmmtools`, using a time step of  $\Delta t = 2$  fs. All simulations are performed in the NVT-Ensemble, at a temperature of  $T = 300$  K. The friction is set to  $\gamma = 1/\text{ps}$ , non-bonded interactions are calculated using a particle mesh Ewald scheme [61] with a cutoff of 1 nm and an error tolerance of 0.0005. We constrained the length of all bonds involving hydrogen atoms.

## G. TPS

All TPS simulations were carried out using a customized version of the `openpathsampling` python package [51] together with custom python code. For alanine dipeptide the states *A* and *B* are defined in terms of the dihedral angles  $\psi$  and  $\phi$ . For both states  $\phi$  must lie in the range  $[-\pi, 0]$ . For state *A*  $\psi$  must lie in the range  $[\frac{2}{3}\pi, \frac{10}{9}\pi]$ , while for state *B*  $\psi \in [\frac{5}{18}\pi, \frac{1}{6}\pi]$ . We consider LiCl ions bound if  $r \leq 0.24$  nm, and as unbound if  $r \geq 0.47$  nm. We obtained initial TPs by standard MD at a temperature of  $T = 400$  K. New shooting configurations  $\mathbf{x}_{\text{sp}}$  were selected from the last accepted TP with probability reported in Eq. (4) with  $\gamma = 1$ .

We used custom code written using NumPy [62], SciPy [63], IPython [64], Matplotlib [65], Cython [66], SymPy [67], and mdtraj [68] to analyze and visualize data. Molecular representations were made with VMD [69].

## ACKNOWLEDGMENTS

The authors acknowledge Dr. Anna Kreshuk, Profs. Peter Bolhuis, Christoph Dellago, Andrew Ferguson, and Mark E. Tuckerman, for stimulating discussions, and the Open Path Sample community, in particular Dr. David Swenson, for discussions and technical support. This work was supported by the Max Planck Society.

- [1] B. Peters, *Reaction Rate Theory and Rare Events* (Elsevier B.V., 2017).
- [2] C. Abrams and G. Bussi, *Entropy* **16**, 163 (2013), arXiv:arXiv:1401.0387v1.
- [3] M. a. Rohrdanz, W. Zheng, and C. Clementi, *Annu. Rev. Phys. Chem.* **64**, 295 (2013).
- [4] B. Peters, *Annu. Rev. Phys. Chem.* **67**, 669 (2016).
- [5] C. Bishop, *Pattern Recognition and Machine Learning* (Springer New York, New York, New York, USA, 2006).
- [6] Y. Lecun, Y. Bengio, and G. Hinton, *Nature* **521**, 436 (2015), arXiv:arXiv:1312.6184v5.
- [7] I. Goodfellow, Y. Bengio, and A. Courville, *Deep Learning* (MIT Press, 2016).
- [8] C. Dellago, P. G. Bolhuis, F. S. Csajka, and D. Chandler, *J. Chem. Phys.* **108**, 1964 (1998).
- [9] P. G. Bolhuis, D. Chandler, C. Dellago, and P. L. Geissler, *Annu. Rev. Phys. Chem.* **53**, 291 (2002).
- [10] G. Hummer, *J. Chem. Phys.* **120**, 516 (2004).
- [11] B. Peters and B. L. Trout, *J. Chem. Phys.* **125**, 054108 (2006).
- [12] A. Ma and A. R. Dinner, *J. Phys. Chem. B* **109**, 6769 (2005).
- [13] H. Jung, K.-i. Okazaki, and G. Hummer, *J. Chem. Phys.* **147**, 152716 (2017).
- [14] S. H. Northrup, M. R. Pear, C. Y. Lee, J. A. McCammon, and M. Karplus, *Proc. Natl. Acad. Sci. USA* **79**, 4035 (1982).
- [15] R. Du, V. S. Pande, A. Y. Grosberg, T. Tanaka, and E. S. Shakhnovich, *J. Chem. Phys.* **108**, 334 (1998).
- [16] R. B. Best and G. Hummer, *Proc. Nat. Acad. Sci. USA* **102**, 6732 (2005).
- [17] J. Behler and M. Parrinello, *Phys. Rev. Lett.* **98**, 146401 (2007).
- [18] P. Geiger and C. Dellago, *J. Chem. Phys.* **139**, 164105 (2013).
- [19] J. Behler, *J. Phys. Condens. Matter* **26**, 183001 (2014).
- [20] E. Schneider, L. Dai, R. Q. Topper, C. Drechsel-Grau, and M. E. Tuckerman, *Phys. Rev. Lett.* **119**, 150601 (2017).
- [21] H. Sidky and J. K. Whitmer, *J. Chem. Phys.* **148**, 104111 (2018), arXiv:1712.02840.
- [22] K. T. Butler, D. W. Davies, H. Cartwright, O. Isayev, and A. Walsh, *Nature* **559**, 547 (2018).
- [23] W. Chen, A. R. Tan, and A. L. Ferguson, *J. Chem. Phys.* **149**, 72312 (2018).
- [24] C. X. Hernández, H. K. Wayment-Steele, M. M. Sultan, B. E. Husic, and V. S. Pande, *Phys. Rev. E* **97**, 1 (2018), arXiv:1711.08576.
- [25] J. M. L. Ribeiro, P. Bravo, Y. Wang, and P. Tiwary, *J. Chem. Phys.* **149** (2018), 10.1063/1.5025487, arXiv:1802.03420.
- [26] J. Zhang and M. Chen, *Phys. Rev. Lett.* **121**, 10601 (2018), arXiv:1705.07414.
- [27] C. Wehmeyer and F. Noé, *J. Chem. Phys.* **148**, 241703 (2018).
- [28] A. Mardt, L. Pasquali, H. Wu, and F. Noé, *Nat. Commun.* **9**, 1 (2018), arXiv:1710.06012.
- [29] S. J. Kemp, P. Zaradic, and F. Hansen, *Ecol. Modell.* **204**, 326 (2007).
- [30] M. Schmidt and H. Lipson, *Science* **324**, 81 (2009).
- [31] D. Izzo, F. Biscani, and A. Mereta, *Lect. Notes Comput. Sci. (including Subser. Lect. Notes Artif. Intell. Lect. Notes Bioinformatics)* **10196 LNCS**, 35 (2016), arXiv:1611.04766.
- [32] J. Parsons, J. B. Holmes, J. M. Rojas, J. Tsai, and C. E. M. Strauss, *J. Comput. Chem.* **26**, 1063 (2005).
- [33] J. Behler, *J. Chem. Phys.* **134**, 074106 (2011).
- [34] P. G. Bolhuis, C. Dellago, and D. Chandler, *Proc. Natl. Acad. Sci. U. S. A.* **97**, 5877 (2000).
- [35] P. L. Geissler, C. Dellago, and D. Chandler, *J. Phys. Chem. B* **103**, 3706 (1999).
- [36] M. Grünwald, C. Dellago, and P. L. Geissler, *J. Chem. Phys.* **129** (2008), 10.1063/1.2978000, arXiv:0807.2348.
- [37] R. G. Mullen, J.-E. Shea, and B. Peters, *J. Chem. Theory Comput.* **11**, 2421 (2015).
- [38] G. Menzl, A. Singraber, and C. Dellago, *Faraday Discuss.* **195**, 345 (2016).
- [39] L. Mones, N. Bernstein, and G. Csányi, *J. Chem. Theory Comput.* **12**, 5100 (2016).
- [40] A. K. Faradjian and R. Elber, *J. Chem. Phys.* **120**, 10880 (2004).
- [41] R. J. Allen, C. Valeriani, and P. Rein Ten Wolde, *J. Phys. Condens. Matter* **21** (2009), 10.1088/0953-8984/21/46/463102, arXiv:0906.4758.
- [42] J. Kästner, *Wiley Interdiscip. Rev. Comput. Mol. Sci.* **1**, 932 (2011).
- [43] A. Grossfield, “WHAM: the weighted histogram analysis method,”.
- [44] A. Laio and M. Parrinello, *Proc. Natl. Acad. Sci.* **99**, 12562 (2002).
- [45] A. P. Bartók, R. Kondor, and G. Csányi, *Phys. Rev. B* **87**, 184115 (2013).
- [46] A. P. Bartók, S. De, C. Poelking, N. Bernstein, J. R. Kermode, G. Csányi, and M. Ceriotti, *Sci. Adv.* **3**, e1701816 (2017).
- [47] M. Chen, T.-Q. Yu, and M. E. Tuckerman, *Proc. Natl. Acad. Sci. U. S. A.* **112**, 3235 (2015).
- [48] J. Rogal and P. G. Bolhuis, *J. Chem. Phys.* **129**, 224107 (2008).
- [49] P. Király, D. J. Kiss, and G. Tóth, *J. Chem. Phys.* **148** (2018), 10.1063/1.5007032.
- [50] T. Wu and M. Tegmark, (2018), arXiv:1810.10525v2, arXiv:1810.10525.
- [51] D. W. H. Swenson, J.-H. Prinz, F. Noe, J. D. Chodera, and P. G. Bolhuis, *J. Chem. Theory Comput.*, acs.jctc.8b00627 (2018).
- [52] B. Leimkuhler and C. Matthews, *Appl. Math. Res. Express* **2013**, 34 (2012), arXiv:1203.5428.
- [53] G. Klambauer, T. Unterthiner, A. Mayr, and S. Hochreiter, in *Advances in Neural Information Processing Systems 30*, edited by I. Guyon, U. V. Luxburg, S. Bengio, H. Wallach, R. Fergus, S. Vishwanathan, and R. Garnett (Curran Associates, Inc., 2017).
- [54] J. Lehman and K. O. Stanley, in *Proc. 12th Annu. Conf. Genet. Evol. Comput. - GECCO '10*, Vol. 33 (ACM Press, New York, New York, USA, 2010) p. 103, arXiv:1412.6980.
- [55] F. Chollet and Others, “Keras,” (2015).
- [56] K. Lindorff-Larsen, S. Piana, K. Palmo, P. Maragakis, J. L. Klepeis, R. O. Dror, and D. E. Shaw, *Proteins* **78**, 1950 (2010).
- [57] W. L. Jorgensen, J. Chandrasekhar, J. D. Madura, R. W.

- Impey, and M. L. Klein, *J. Chem. Phys.* **79**, 926 (1983).
- [58] I. S. Joung and T. E. Cheatham, *J. Phys. Chem. B* **112**, 9020 (2008).
- [59] P. Eastman, J. Swails, J. D. Chodera, R. T. McGibbon, Y. Zhao, K. A. Beauchamp, L. P. Wang, A. C. Simmonett, M. P. Harrigan, C. D. Stern, R. P. Wiewiora, B. R. Brooks, and V. S. Pande, *PLoS Comput. Biol.* **13**, 1 (2017).
- [60] D. A. Sivak, J. D. Chodera, and G. E. Crooks, *J. Phys. Chem. B* **118**, 6466 (2014).
- [61] U. Essmann, L. Perera, M. L. Berkowitz, T. Darden, H. Lee, and L. G. Pedersen, *J Chem Phys* **103**, 8577 (1995).
- [62] T. E. Oliphant, *Guide to NumPy*, 2nd ed. (CreateSpace Independent Publishing Platform, USA, 2015).
- [63] E. Jones, T. Oliphant, P. Peterson, and Others, “SciPy: Open source scientific tools for Python,” .
- [64] F. Perez and B. E. Granger, *Comput. Sci. Eng.* **9**, 21 (2007).
- [65] J. D. Hunter, *Comput. Sci. Eng.* **9**, 90 (2007).
- [66] S. Behnel, R. Bradshaw, C. Citro, L. Dalcin, D. S. Seljebotn, and K. Smith, *Comput. Sci. Eng.* **13**, 31 (2011).
- [67] A. Meurer, C. P. Smith, M. Paprocki, O. Čertík, S. B. Kirpichev, M. Rocklin, A. Kumar, S. Ivanov, J. K. Moore, S. Singh, T. Rathnayake, S. Vig, B. E. Granger, R. P. Muller, F. Bonazzi, H. Gupta, S. Vats, F. Johansson, F. Pedregosa, M. J. Curry, A. R. Terrel, Š. Roučka, A. Saboo, I. Fernando, S. Kulal, R. Cimrman, and A. Scopatz, *PeerJ Comput. Sci.* **3**, e103 (2017).
- [68] R. T. McGibbon, K. A. Beauchamp, M. P. Harrigan, C. Klein, J. M. Swails, C. X. Hernández, C. R. Schwantes, L. P. Wang, T. J. Lane, and V. S. Pande, *Biophys. J.* **109**, 1528 (2015).
- [69] W. Humphrey, A. Dalke, and K. Schulten, *J. Mol. Graph.* **14**, 33 (1996).

# Supporting Information: Artificial Intelligence Assists Discovery of Reaction Coordinates and Mechanisms from Molecular Dynamics Simulations

Hendrik Jung,<sup>1,\*</sup> Roberto Covino,<sup>1,\*</sup> and Gerhard Hummer<sup>1,2,†</sup>

<sup>1</sup>*Department of Theoretical Biophysics,  
Max Planck Institute of Biophysics,  
60438 Frankfurt am Main, Germany.*

<sup>2</sup>*Institute of Biophysics, Goethe University,  
60438 Frankfurt am Main, Germany.*

## Abstract

Exascale computing holds great opportunities for molecular dynamics (MD) simulations. However, to take full advantage of the new possibilities, we must learn how to focus computational power on the discovery of complex molecular mechanisms, and how to extract them from enormous amounts of data. Both aspects still rely heavily on human experts, which becomes a serious bottleneck when a large number of parallel simulations have to be orchestrated to take full advantage of the available computing power. Here, we use artificial intelligence (AI) both to guide the sampling and to extract the relevant mechanistic information. We combine advanced sampling schemes with statistical inference, artificial neural networks, and deep learning to discover molecular mechanisms from MD simulations. Our framework adaptively and autonomously initializes simulations and learns the sampled mechanism, and is thus suitable for massively parallel computing architectures. We propose practical solutions to make the neural networks interpretable, as illustrated in applications to molecular systems.

---

\* These authors contributed equally to this work.

† Corresponding author: gerhard.hummer@biophys.mpg.de

## I. MODEL SYSTEM

The functional form of the model energy surface shown in Fig. 1 is

$$\begin{aligned}
 V(x, y) = & \sigma_x x^6 + \sigma_y y^6 \\
 & + \epsilon_A \exp \left( -\alpha_x^A (x - x_0^A)^2 - \alpha_y^A (y - y_0^A)^2 \right) \\
 & + \epsilon_B \exp \left( -\alpha_x^B (x - x_0^B)^2 - \alpha_y^B (y - y_0^B)^2 \right)
 \end{aligned} \tag{1}$$

where  $\sigma_x$  and  $\sigma_y$  are parameters controlling the steepness of the outer boundary, and  $\epsilon_A$  and  $\epsilon_B$  control the depth of state  $A$  and  $B$ , respectively. The states have minima located at positions  $(x_0^A, y_0^A)$  and  $(x_0^B, y_0^B)$ , with extensions controlled by  $(\alpha_x^A, \alpha_y^A)$  and  $(\alpha_x^B, \alpha_y^B)$ . We expressed energies in inverse temperature units,  $\beta = (\text{k}_B T)^{-1}$ , with  $\text{k}_B$  the Boltzmann constant and  $T$  the absolute temperature. We performed simulations with constants  $\sigma_x = 2 \beta^{-1}$  and  $\sigma_y = 10 \beta^{-1}$ , and  $\alpha_x^A = \alpha_y^A = \alpha_x^B = \alpha_y^B = 12$ . The barrier height was set to approximately  $7\beta^{-1}$  by choosing  $\epsilon_A = \epsilon_B = -7 \beta^{-1}$ . The states  $A$  and  $B$  are located at  $(x_0^A = -0.75, y_0^A = -0.5)$  and  $(x_0^B = 0.75, y_0^B = 0.5)$ .

## II. TRANSITION PATH SAMPLING

If transition path (TP) shooting produces a new TP  $\chi^{(i)}$ , we accept or reject it with probability  $p_{\text{acc}}$  given by the Metropolis-Hastings criterion [1].

$$p_{\text{acc}}(\chi^{(i)} | \chi^{(i-1)}(\tau')) = \min \left( 1, \frac{p_{\text{sel}}(\mathbf{x}_{\text{sp}} | \chi^{(i)})}{p_{\text{sel}}(\mathbf{x}_{\text{sp}} | \chi^{(i-1)}(\tau'))} \right), \tag{2}$$

where  $p_{\text{sel}}(\mathbf{x}_{\text{sp}} | \chi^{(i)})$  is the probability to select a particular shooting configuration from the TP.

## III. DEEP LEARNING

We write the unknown reaction coordinate  $q(\mathbf{x})$  in terms of the following artificial neural network (ANN):

$$\begin{aligned}
 q(\mathbf{x}) = & q_{\text{ANN}}(\mathbf{x} | \mathbf{w}) \\
 \equiv & \sum_{j_K=1}^{m_K} h \left( \dots h \left\{ \sum_{j_2=1}^{m_2} h \left[ \sum_{j_1=1}^{m_1} h \left( \sum_{\alpha=1}^n x_\alpha w_{\alpha, j_1}^0 + w_{0, j_1}^0 \right) w_{j_1, j_2}^1 + w_{0, j_2}^1 \right] w_{j_2, j_3}^2 + w_{0, j_3}^2 \right\} \dots \right) w_{j_K}^K + w_0^K,
 \end{aligned} \tag{3}$$



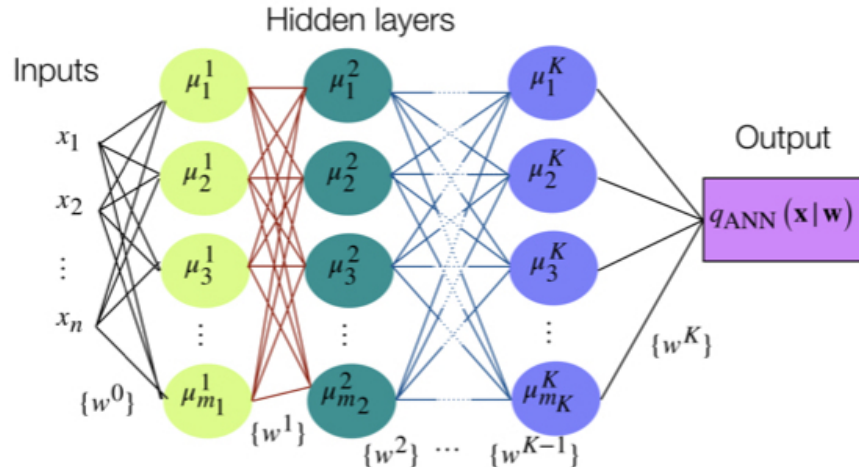


Figure 1. Schematic representation of the ANN used for deep learning.

which represents a network (Figure 1) that takes  $x_1, x_2, \dots, x_n$  different inputs, with  $K$  hidden layers containing each  $m_1, m_2, \dots, m_K$  different nodes. The weight matrix  $\mathbf{w}$ , i.e., the fitting parameters, defines the connections between nodes, with  $w_{ik}^j$  connecting node  $i$  of layer  $j$  with node  $k$  of layer  $j + 1$ . The “activation” function  $h$  is a non linear function mimicking the threshold firing behavior of biological neurons.

#### IV. SYMBOLIC REGRESSION

After determining the most relevant inputs we use symbolic regression, and in particular differentiable Cartesian genetic programming, to approximate the trained ANN with a simple expression [2]. We employ a 1+4 evolutionary strategy for 250 generations where every change in the genome of an offspring is followed by 2500 Newton steps in the weight space of that expression. We add a regularization term  $\lambda n$  where  $n$  is proportional to the number of active genes to avoid overfitting. We test regularization values of  $\lambda \in [0.005, 0.001, 0.01]$ .

---

[1] H. Jung, K.-i. Okazaki, and G. Hummer, *J. Chem. Phys.* **147**, 152716 (2017).

[2] D. Izzo, F. Biscani, and A. Mereta, *Lect. Notes Comput. Sci. (including Subser. Lect. Notes Artif. Intell. Lect. Notes Bioinformatics)* **10196 LNCS**, 35 (2016), arXiv:1611.04766.

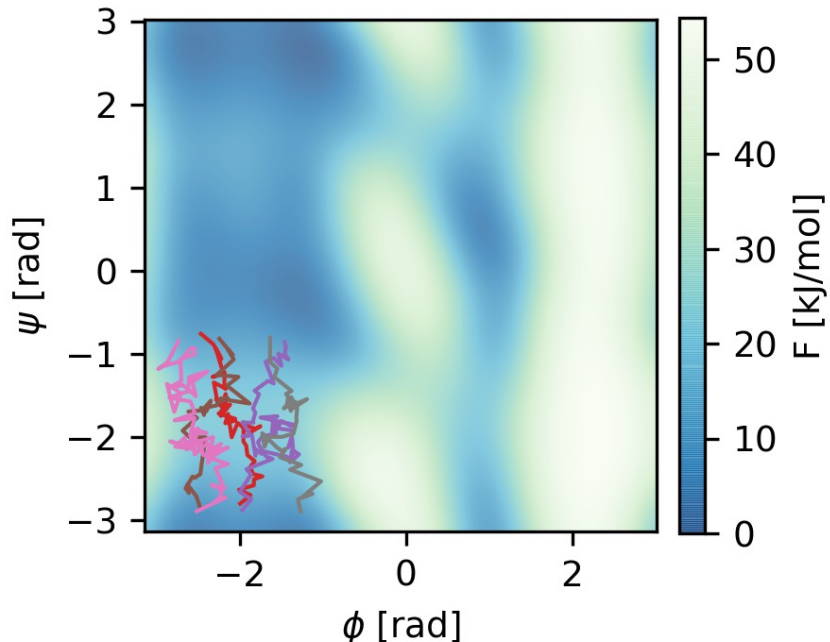


Figure 2. Free energy surface of alanine dipeptide as a function of the main dihedral angles  $\phi$  and  $\psi$ . In the lower left corner we report some representative TPs that cross the high energy barrier, which correspond to a rotation of  $\psi$ . The free energy was obtained by using metadynamics.

Table I. Input relevance analysis for alaine dipeptide. The first 4 most relevant input coordinates and their range of values. All symmetry functions probe the oxygens of water using the parameters in brackets, the subscript to  $G$  indicates the index of the central atom. Index 5 is the oxygen of the acetyl involved in the peptide bond. Index 12 is the 3 symmetry related hydrogen atom of the methyl-group of alanine and index 16 is the nitrogen of the methylamide.

| Index | Definition and range  | Normalized relevance $r(x_i)$ |
|-------|---|-------------------------------|
| $x_1$ | $\tilde{\psi} = 0.5(\cos(\psi + \pi) + 1) \in [0.1306, 0.9778]$                   | 1.00                          |
| $x_2$ | $G_5^5(\eta = 40, r_s = 0.175, \zeta = 64, \lambda = -1) \in [0.0032, 1.7550]$    | 0.07                          |
| $x_3$ | $G_{12}^5(\eta = 40, r_s = 0.175, \zeta = 64, \lambda = -1) \in [0.0035, 1.3719]$ | 0.05                          |
| $x_4$ | $G_{16}^5(\eta = 40, r_s = 0.175, \zeta = 64, \lambda = -1) \in [0.0053, 1.5534]$ | 0.05                          |

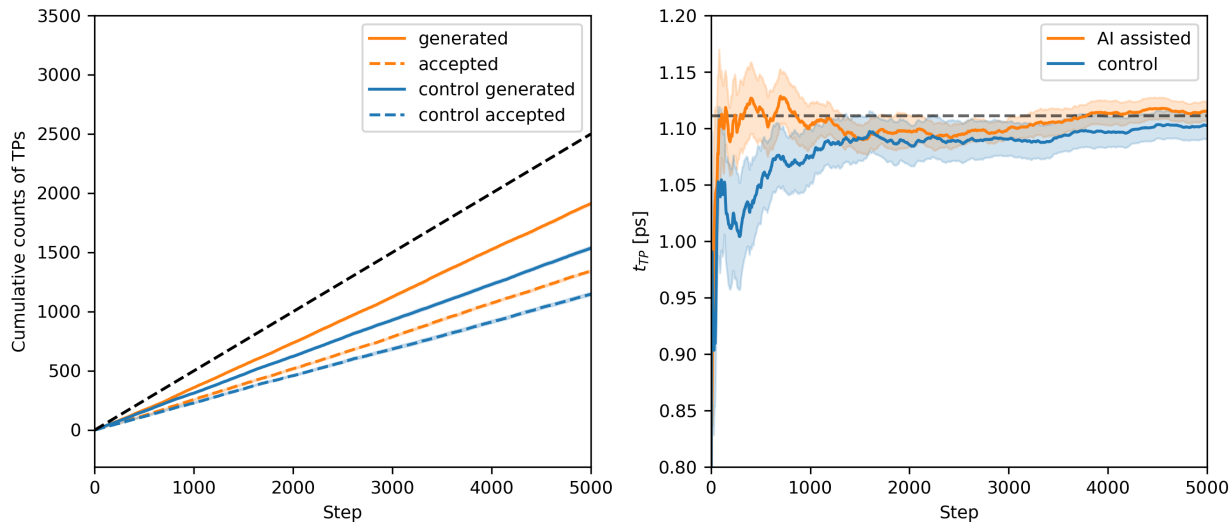


Figure 3. TP sampling results for alanine dipeptide. (Left) Cumulative count of generated (continuous line) and accepted (dashed line) TPs in AI-assisted MD simulations (orange) and standard control Transition Path Sampling (TPS) (blue). Each line shows the average over 10 independent runs. The standard error of the mean is smaller than the thickness of the lines. The black dashed line represent the theoretical maximum for generation of TPs. (Right) Convergence of TP time. Running average for AI-assisted MD simulations (orange) and control TPS simulation (blue). Each line shows the average over 10 independent runs. The shaded area is given by the standard error of the mean. The black dashed line represent the reference value calculated in a long control TPS simulation.

Table II. Symbolic regression results for alanine dipeptide. We used as input the first or the four most important coordinates as shown in Table I. Due to the regularization we applied, some input coordinates are not part of the final converged expressions. We used every 10th shooting configurations extracted from the TPS simulation as training set for the symbolic regression. The loss values  $L_{\text{ANN}}$  and  $L_{\text{SR}}$  were calculated for the reduced set of points and correspond to the test loss per shooting configuration of the ANN and symbolic regression expression respectively. For every parameter combination the symbolic regression was repeated three times to quantify the stability of the results.

| $L_{\text{ANN}}$ | Selected coordinates | $\lambda$ | $L_{\text{SR}}$ | Frequency  | Final expression   |
|------------------|----------------------|-----------|-----------------|--|--|
| 1.031            | 1                    | 0.01      | 1.057           | 3/3  | $q_{\text{SR}} = -5.241\tilde{\psi} - 1.865 \ln(\tilde{\psi}) + 2.550$ |
|                  |                      | 0.005     | 1.057           | 3/3  | $q_{\text{SR}} = -5.241\tilde{\psi} - 1.865 \ln(\tilde{\psi}) + 2.550$ |
|                  | 0.001                | 1.057     | 2/3             | $q_{\text{SR}} = -5.241\tilde{\psi} - 1.865 \ln(\tilde{\psi}) + 2.550$ |  |
|                  |                      | 1.049     | 1/3             | $q_{\text{SR}} = -8.377\tilde{\psi} + 5.424$                           |  |
|                  | 4                    | 0.01      | 1.051           | 2/3  | $q_{\text{SR}} = -8.384\tilde{\psi} + 5.622 \exp(-0.285x_3)$           |
|                  |                      |           | 1.053           | 1/3  | $q_{\text{SR}} = -1.438x_3 - 5.153 \ln(\tilde{\psi}) - 2.172$          |
|                  |                      | 0.001     | 1.051           | 2/3  | $q_{\text{SR}} = -8.384\tilde{\psi} + 5.622 \exp(-0.285x_3)$           |
|                  |                      |           | 1.053           | 1/3  | $q_{\text{SR}} = -1.438x_3 - 5.153 \ln(\tilde{\psi}) - 2.172$          |

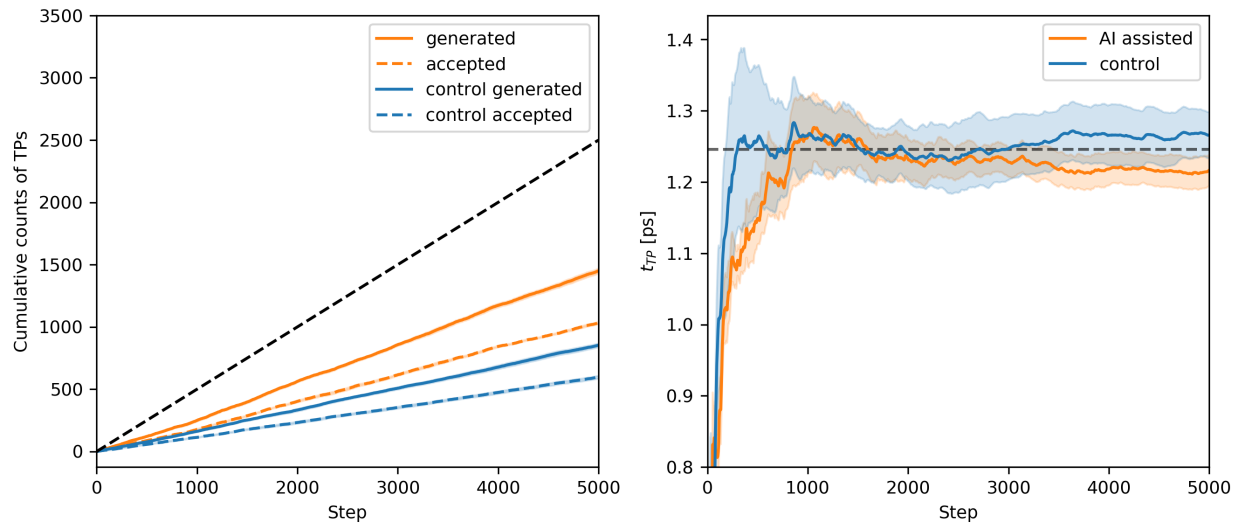


Figure 4. TP sampling results for LiCl. (Left) Cumulative count of generated (continuous line) and accepted (dashed line) TPs in AI-assisted MD simulations (orange) and standard control TPS (blue). Each line shows the average over 10 independent runs. The standard error of the mean is smaller than the thickness of the lines. The black dashed line represent the theoretical maximum for generation of TPs. (Right) Convergence of TP time. Running average for AI-assisted MD simulations (orange) and control TPS simulation (blue). Each line shows the average over 10 independent runs. The shaded area is given by the standard error of the mean. The black dashed line represent the reference value calculated in a long control TPS simulation.



Table III. Input relevance analysis for LiCl. Range of values of the most relevant coordinates. The symmetry functions are centered on the central atom indicated by the subscript and use the parameters in brackets to probe for the solvent species in square brackets.

| Index    | Definition and range  | Normalized relevance $r(x_i)$ |
|----------|---|-------------------------------|
| $x_1$    | $G_{\text{Li}}^5(\eta = 160, r_s = 0.7, \zeta = 4, \lambda = -1)[\text{Cl}] \in [0.0, 0.491]$     | 1.00                          |
| $x_2$    | $G_{\text{Li}}^5(\eta = 160, r_s = 0.7, \zeta = 64, \lambda = -1)[\text{Cl}] \in [0.0, 0.417]$    | 0.78                          |
| $x_3$    | $G_{\text{Li}}^5(\eta = 160, r_s = 0.625, \zeta = 16, \lambda = -1)[\text{Cl}] \in [0.0, 0.007]$  | 0.68                          |
| $x_4$    | $G_{\text{Li}}^5(\eta = 160, r_s = 0.625, \zeta = 4, \lambda = -1)[\text{Cl}] \in [0.0, 0.343]$   | 0.45                          |
| $x_5$    | $G_{\text{Cl}}^5(\eta = 160, r_s = 0.7, \zeta = 4, \lambda = 1)[\text{Li}] \in [0.0, 6.940]$      | 0.44                          |
| $x_6$    | $G_{\text{Cl}}^2(\eta = 300, r_s = 0.4)[\text{Li}] \in [0.0, 5.072]$                              | 0.38                          |
| $x_7$    | $G_{\text{Cl}}^5(\eta = 160, r_s = 0.7, \zeta = 2, \lambda = 1)[\text{Li}] \in [0.0, 5.678]$      | 0.32                          |
| $x_8$    | $G_{\text{Cl}}^5(\eta = 160, r_s = 0.625, \zeta = 4, \lambda = -1)[\text{Li}] \in [0.0, 0.971]$   | 0.27                          |
| $x_9$    | $G_{\text{Li}}^5(\eta = 160, r_s = 0.175, \zeta = 16, \lambda = -1)[\text{O}] \in [0.061, 6.713]$ | 0.23                          |
| $x_{10}$ | $G_{\text{Cl}}^5(\eta = 160, r_s = 0.475, \zeta = 4, \lambda = -1)[\text{Li}] \in [0.0, 7.666]$   | 0.19                          |
| $x_{69}$ | $r_{\text{LiCl}} \in [0.240, 0.470]$  | 0.006                         |

Table IV. Symbolic regression results for LiCl. We use as input the 3 or 10 most important coordinates and the interionic distance as shown in Table III. Due to the regularization we apply, some input coordinates are not part of the final converged expressions. We used every 10th shooting configurations extracted from the TPS simulation as training set for the symbolic regression. The loss values  $L_{\text{ANN}}$  and  $L_{\text{SR}}$  are calculated for the reduced set of points and correspond to the test loss per shooting point of the ANN and symbolic regression expression respectively. For every parameter combination the symbolic regression was repeated three times to quantify the stability of the results.

| $L_{\text{ANN}}$ | Selected coordinates   | $\lambda$ | $L_{\text{SR}}$ | Frequency  | Final expression   |
|------------------|------------------------|-----------|-----------------|--|--|
|                  |                        | 0.01      | 0.757           | 3/3  | $q_{\text{SR}} = 29.837r_{\text{LiCl}} - 8.485 \exp(-0.728x_1)$                                |
|                  | 3 + $r_{\text{LiCl}}$  | 0.005     | 0.757           | 3/3  | $q_{\text{SR}} = 29.837r_{\text{LiCl}} - 8.485 \exp(-0.728x_1)$                                |
|                  |                        |           | 0.757           | 1/3  | $q_{\text{SR}} = 29.837r_{\text{LiCl}} - 8.485 \exp(-0.728x_1)$                                |
|                  |                        | 0.001     |                 |  | $q_{\text{SR}} = 29.896r_{\text{LiCl}} - 8.518 \exp(-0.617x_1)$<br>$+ 4.953x_2$                |
|                  |                        |           | 0.754           | 1/3  |  |
| 0.706            |                        |           | 0.746           | 1/3  | $q_{\text{SR}} = 30.115r_{\text{LiCl}} \exp(0.996x_2)$<br>$- 8.973 \sin(1.260 \exp(3.269x_1))$ |
|                  | 10 + $r_{\text{LiCl}}$ |           | 0.753           | 1/3  | $q_{\text{SR}} = 29.592r_{\text{LiCl}} - 8.204 \exp(0.028x_9)$<br>$+ 10.093x_4$                |
|                  |                        | 0.01      |                 |  |  |
|                  |                        |           | 0.757           | 1/3  | $q_{\text{SR}} = 29.837r_{\text{LiCl}} - 8.405 \exp(-0.728x_1)$                                |
|                  |                        |           | 0.761           | 1/3  | $q_{\text{SR}} = 28.993r_{\text{LiCl}} - 0.182 \ln(x_9) - 8.273$                               |
|                  |                        | 0.005     |                 |  |  |
|                  |                        |           | 0.758           | 2/3  | $q_{\text{SR}} = 29.913r_{\text{LiCl}} - 8.473 \exp(-1.158x_4)$                                |
|                  |                        |           | 0.757           | 1/3  | $q_{\text{SR}} = 29.837r_{\text{LiCl}} - 8.485 \exp(-0.728x_1)$                                |
|                  |                        |           |                 | 0.751  | 1/3  |
|                  | 0.001                  |           |                 |  |  |
|                  |                        | 0.751     | 1/3             | $q_{\text{SR}} = 29.550r_{\text{LiCl}} - 8.214 \exp(0.031x_9)$<br>$+ 6.767x_1$ |  |
|                  |                        | 0.757     | 1/3             | $q_{\text{SR}} = 29.837r_{\text{LiCl}} - 8.485 \exp(-0.728x_1)$                |  |